Engineering Geology 268 (2020) 105526

Contents lists available at ScienceDirect

Engineering Geology

journal homepage: www.elsevier.com/locate/enggeo

Sub-surface structures and site effects extracted from ambient noise in metropolitan Guangzhou, China

Shuang Wang[a,b,d], Xinlei Sun[a,*], Lanbo Liu[c,d], Jianye Zong[a,b]

[a] State Key Laboratory of Isotope Geochemistry, Guangzhou Institute of Geochemistry, Chinese Academy of Sciences, Guangzhou 510640, China
[b] University of Chinese Academy of Sciences, Beijing 100049, China
[c] Department of Civil & Environmental Engineering, University of Connecticut, CT 06269, USA
[d] Department of Geosciences, University of Connecticut, CT 06269, USA

ARTICLE INFO

Keywords:
Ambient noise
Horizontal to vertical spectral ratio (HVSR)
Tomography
Site effects
Shear wave velocity
Guangzhou metropolitan area

ABSTRACT

In this paper, ambient noise is used to investigate near-surface structures and site effects in metropolitan Guangzhou. We deployed 94 short period stations across Guangzhou area, and later a dense linear array across the Shougouling Fault (SF). Using more than one month's continuous data, we invert three-dimensional shear wave velocity structures of Guangzhou area via ambient noise tomography. Results show low velocity near the Guangzhou-Conghua Fault (GCF), Shougouling Fault (SF), and beneath the alluvial plain in the south region. Meanwhile, high-velocity anomalies are beneath the mountain area in northeastern region. Moreover, we obtain the sediment thickness and sub-surface shear wave velocity structures around the Shougouling Fault (SF) by horizontal to vertical spectral ratio (HVSR) method. HVSR results show a significant shift in the thickness of the sedimentary layer across the SF. Shear wave velocity derived from HVSR curves has a consistent trend of variation with the sediment thickness. Our results provide a better understanding of sub-surface structures of metropolitan Guangzhou, and can be served as a reference model for geological disaster migration prediction in the city.

1. Introduction

Guangzhou City is one of the largest transportation, tourist, financial, trade and cultural centers in south China. It has been experiencing rapid economy and population growth for the last few decades. With the acceleration of urbanization and rapid development of infrastructure constructions, geological hazards, such as sinkholes, landslides and debris flows, have occurred frequently (Liu et al., 2004; Liu et al., 2005). Comprehensive survey of underground structures in the Guangzhou area is thus highly demanded as it is important for geological hazard prevention and mitigation.

Located in the central part of the Central Guangdong Depression of the South China Fold System, Guangzhou City has experienced multiphase tectonic movements in geological times, such as the Caledonian movement in the Paleozoic era and the Yanshanian movements in the Mesozoic era (mainly in the Jurassic period), as well as the Hercynian movements in the late Cenozoic era (mainly in the Neogene period) (Cheng, 2012). There are three main fault systems across the Guangzhou area: The NE-SW oriented Guangzhou-Conghua Fault (GCF), the EW running Shougouling Fault (SF), and the NW-SE trending Baini-Shawan Fault (BSF) (Fig. 1). The GCF and SF constitute the basic tectonic framework of Guangzhou area. The GCF controls the distribution of geothermal and hot springs, the formation of landscapes and the occurrence of seismic activities in Guangzhou (Yan, 1989). The currently active Shougouling fault (SF) acts as the northern boundary of the Pearl River Delta and controls the sedimentation and development of the delta basin (Chen et al., 2000).

According to the geological settings, Guangzhou is generally divided into three parts. North and northeastern Guangzhou are mountain area, including the Baiyun and Maofeng mountains; South Guangzhou are mostly fluvial delta, which come from the Pearl river estuary; Central and Western Guangzhou are mostly basins and karst landform, so sinkholes mostly occur in this area.

In general, the seismic hazard is relatively low in the south China block. However, strong historic earthquakes have occurred in Guangdong province, such as the 1918 Nanao earthquake (M7.3) (Pan et al., 2009) and the Yangjiang earthquake (M6.4) in 1969 (Brantley and Chung, 1991; Liu, 2001); the majority of historical earthquakes in Guangzhou are mainly located in these three fault zones (Deng, 2016). According to previous studies (e.g., Deng, 2016), the activity of the GCF

* Corresponding author.
E-mail address: xsun@gig.ac.cn (X. Sun).

https://doi.org/10.1016/j.enggeo.2020.105526
Received 29 May 2019; Received in revised form 13 December 2019; Accepted 13 February 2020
Available online 14 February 2020

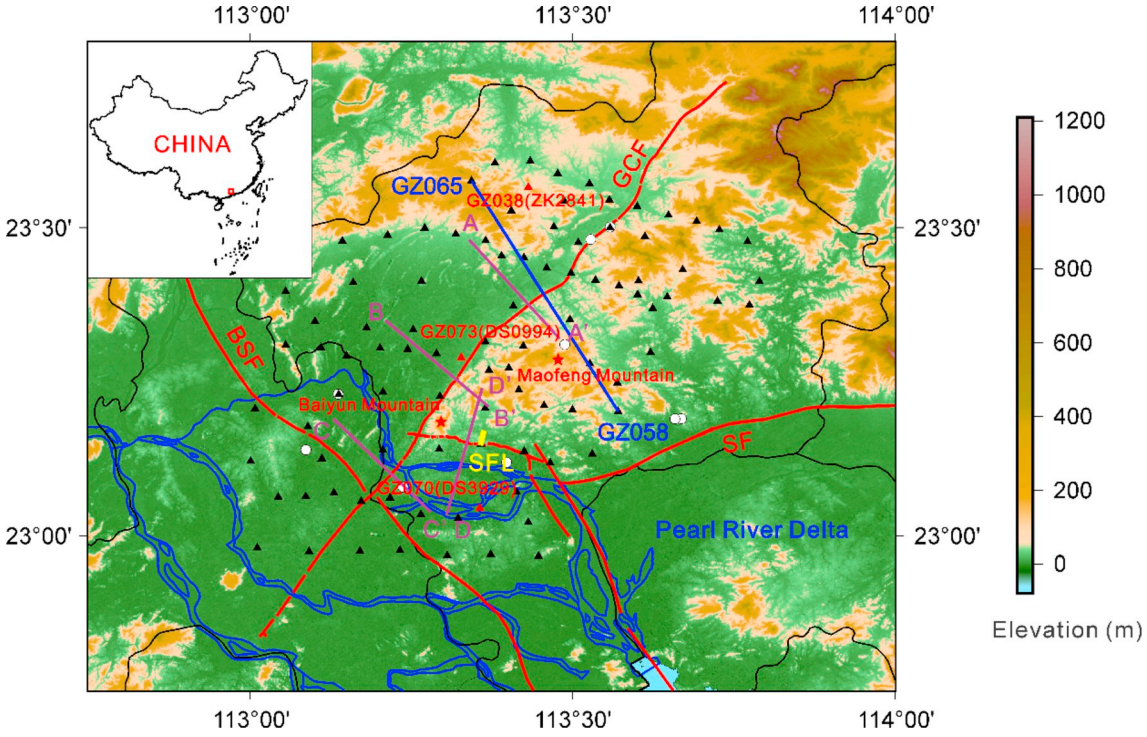

Fig. 1. Distribution of the seismic stations (solid triangles) in Guangzhou City. The background is the topography of the study area, and rivers (blue curved lines), the city boundary (black lines), the fault traces (red lines), the Mountains (red stars), the earthquakes with magnitude greater than 2 (white dots), and the boreholes used in Table 1 (red triangles) are also plotted. The red rectangular of the insert (upper left) shows the location of the research area in China. The short yellow bar labeled as SFL indicates the location of the linear array crossed the Shougouling Fault (SF) discussed in Fig. 2. Station pair of GZ058 and GZ065 is used to extract the empirical Green's function via cross-correlation in Fig. 3. The four magenta lines (AA', BB', CC', and DD') show the location of the tomographic velocity profiles presented in Fig. 11. (For interpretation of the references to colour in this figure legend, the reader is referred to the web version of this article.)

has a tendency to increase gradually from north to south. The southern segment has the highest level of seismicity with higher risk. In recent years, earthquakes with magnitude greater than 2 have occurred in the Guangzhou area (Fig. 1), and several M > 5 earthquakes near Guangdong province also shake the urban Guangzhou area. These earthquakes, as well as other geological hazards, pose great threats to the safety and development of the metropolitan Guangzhou. Thus detailed investigation of the sub-surface structures of Guangzhou is necessary to better understand the potential geological hazards; this can also provide crucial information for future urban planning, environmental management, disaster prevention and mitigation for Guangzhou City.

Previous geological surveys in Guangzhou focused on the ground subsidence and earthquake risks, fault activities and geological disaster mitigation near active faults (Cheng, 2012; Li et al., 2008; Liu et al., 2007a; Liu et al., 2007b; Pan, 1992; Zhou et al., 2009). They used either drilling cores or active sources, and provided clues on the surface geological fault geometry, such as its type, strike, and dip angle (Chen et al., 2000; Cheng, 2012; Deng, 2016). However , these isolated information have limitation to understand the whole geology structure in Guangzhou, and a 3-D sub-surface structure is needed.

The traditional methods of obtaining site effects mainly include theoretical methods (Triantafyllidis et al., 2002; Triantafyllidis et al., 2004) and empirical methods (Boatwright et al., 1991; Borcherdt, 1970). Theoretical methods calculate site effects directly from sub-surface structures, but it is generally difficult to establish a reliable sub-surface model. Empirical methods, on the other hand, obtain site effects by the statistical analysis of the ground motion records; these methods depend on strong earthquake signals generated by natural (Dai, 2015; Geng, 2015) or artificial earthquakes (Jolly et al., 2014; Yoon and Rix, 2009), so their applications are limited in densely populated urban areas lacking of local seismicity. In such case, ambient noise can be an ideal supplementary source for characterizing urban crustal and near-surface structures. Ambient noise surface wave tomography has been proved to be effective in the study of crustal and sub-surface structures (Huang et al., 2010; Li et al., 2016b; Lin et al., 2013; Sun et al., 2010; Wang et al., 2018; Yao et al., 2005), and in recent years it has been applied successfully to the city sub-surface studies. Moreover, with the deployment of dense temporary network, we can achieve the desired resolution through controlling inter-station distances. Using ambient noise data, HVSR can be used for measuring sediment layers and site effects (Bao et al., 2018; Chen et al., 2009; Gosar and Martinec, 2008; Liu et al., 2014; Mundepi and Mahajan, 2010; Panou et al., 2005), and can indicate areas with higher damage potential in urban city.

In this paper, we first introduce the network deployment and data in Section 2. We then apply the ambient noise tomography to study the crustal and sub-surface structures of Guangzhou in Section 3. The investigation of the sediment distribution and site effects across the SF, one of the most important faults transverse the center of Guangzhou, is discussed in Section 4. Finally, we discuss our main findings in term of the sub-surface structures and the implications in Section 5.

2. Seismic station deployment

In January 2018, a temporary seismic network with 94 three-component short-period seismometers was deployed in the Guangzhou area (Fig. 1). The deployment area contains the major portion of the city of Guangzhou, straddled some segments of the three faults (GCF, SF, and BSF) in the city. The inter-station spacing of these seismometers is approximately 3–5 km. The sampling rate for all stations is 100 Hz. Ambient noise data analysis used in this paper includes 35-day continuous seismic records from all these stations.

The SF is one of the most important faults transverse the urban center and plays a significant role in the engineering construction and

Fig. 2. Map of the linear array (SFL) stations (yellow symbols) for SF (red curves) studies. Station 07, 09, 20, 24, 25, 35, 44 and 47 are used in Fig. 12 and Table 1. The boreholes (red stars) used in Table 1 and Fig. 14b are also labeled. (For interpretation of the references to colour in this figure legend, the reader is referred to the web version of this article.)

disaster reduction of Guangzhou. In order to better understand the SF, on August 14, 2018, we also deployed a dense seismic array perpendicular to the SF. This array extends along the Hua-nan Expressway, the main traffic artery in Guangzhou (Fig. 2). It consists of 37 three-component short-period seismometers with the inter-station spacing about 50–80 m. The data sampling rate is 100 Hz. Six hours' continuous data from 0 to 6 AM (the best time window to record coherent ambient noise in urban settings) were recorded.

3. Upper-crust structure imaging from ambient noise tomography

Extracting Green's function from the cross-correlation of ambient noise begins in ultrasonic study (Lobkis and Weaver, 2001). This pioneering technique was quickly applied to seismology (Campillo and Paul, 2003; Snieder, 2004), and ambient noise tomography (ANT) has achieved great development and wide applications at different scales, from continental, regional, local, to a particular building scale in the past decades (Lin et al., 2013; Renalier et al., 2010; Sun et al., 2010; Wang et al., 2018; Yang et al., 2007; Yao et al., 2005). This method does not need conventional signals such as earthquakes and active sources, so it is especially useful in areas with few seismic activities. The flexibility of station deployment makes it even favorable in sub-surface structure investigation in urban area.

The empirical Green's functions (EGF) from ambient noise between station pairs are retrieved following the processing procedure described by Bensen et al. (Bensen et al., 2007). Because we study Rayleigh waves in this study, we only use the vertical component of seismograms. First, we cut the original continuous record of each station into 2 h' segments (our test results show that 2-hour window in optimal), and then remove the mean and trend of the segmented data. Time-domain normalization (running-absolute-mean normalization) and spectral whitening for each segmented data are also performed. Because we use the same type of seismogram, we do not remove the instrument response. Subsequently, we do cross-correlation between all possible station pairs for each segment, and then stack them to improve the signal-to-noise ratio (SNR). Rayleigh waves we obtained show dispersion characteristic clearly (Fig. 3). Fig. 4 shows the EGFs between station GZ058 and all other stations, with clear surface wave propagation at an average velocity of about 3 km/s.

We further do quality control to all the EFGs we obtained. We compute the SNR of each EGF and then select these with SNR greater than 5. For each selected seismogram, we manually select the Rayleigh wave group velocity dispersion curves between 1 and 10 s using multiple filter analysis (Herrmann, 2013). Rayleigh wave group velocity dispersion curves with inter-station distance greater than 2 times of wavelength are selected, which is in general valid in such dense seismic array deployment (Li et al., 2016a; Li et al., 2016b; Yao et al., 2011). The total number of Rayleigh wave dispersion curves at each period is shown in Fig. 5.

We use the Fast Marching Method (FMM) (Rawlinson and Sambridge, 2005) to invert the Rayleigh wave group velocity structures from 1 to 10 s. This method uses a subspace inversion scheme. It assumes local linearity, but iterative inversion allows to account for the non-linear relationship between velocity and travel time. The ray coverage for each period is shown in Fig. 6(a).

In the inversion process, for each period, we set the grid spacing to be 5.5 km × 5.5 km. We tried different smoothing and damping coefficients in checkerboard test (Fig. 6 b). The recovery of the velocity anomalies in checkerboard test are pretty good at different periods, although at long periods (periods ≥7 s), the resolution becomes worse because the reduction of dispersion measurements (Fig. 5).

We apply the same parameters in our real data inversion as in the

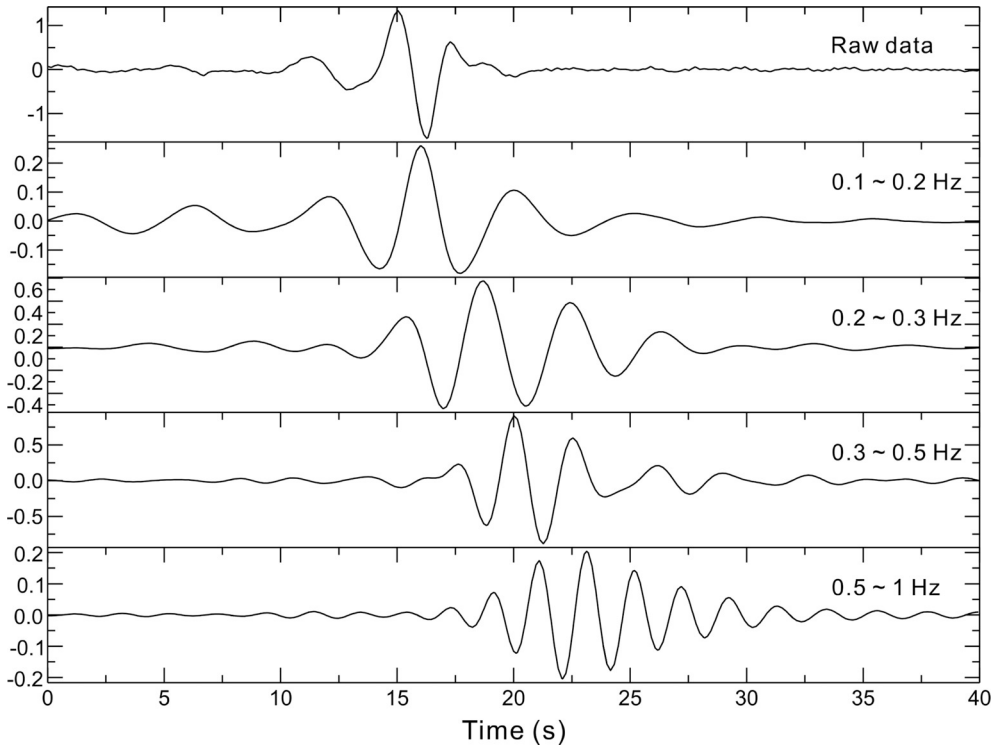

Fig. 3. Example of a 35-day cross-correlation results for station pair GZ058 and GZ065. The location of these two stations are shown in Fig. 1. The raw cross-correlation (top most) is filtered into 4 different frequency bands. The dispersion of Rayleigh wave is clearly observed.

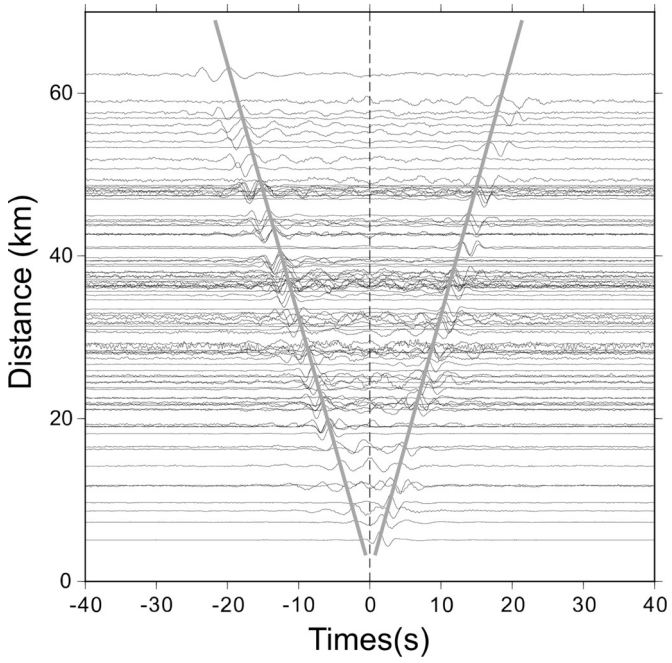

Fig. 4. Example of the empirical Green's functions via cross-correlations between station GZ058 and all other stations using 35 days' ambient noise records. The grey lines indicate the approximate arrival times of Rayleigh wave at different distance with a group velocity of approximately 3 km/s.

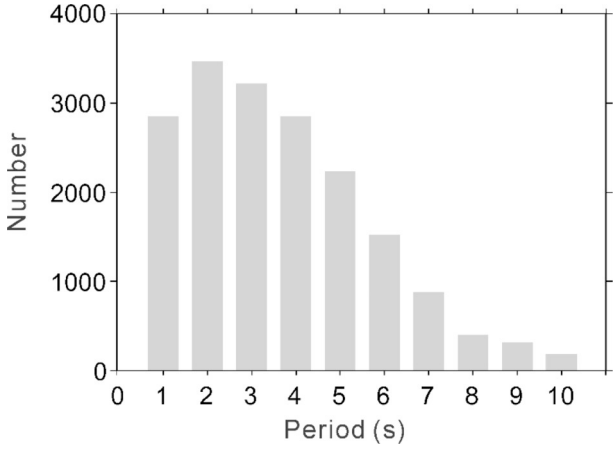

Fig. 5. Histogram of the Rayleigh wave dispersion measurements number as a function of period.

checkerboard test, and get the image of the Rayleigh wave group velocity at different periods (Fig. 7). Finally, for each grid point, we have a dispersion curve from 1 to 10 s.

We performed 1-D sub-surface velocity structure inversion using an iterative, linearized, least squares inversion method (Herrmann, 2013). The initial model consists of 200 layers, and each layer is 50 m thick. So our inversion depth is 10 km. The starting velocity has a uniform velocity of 4 km/s. Some researches (Cheng et al., 2013; Sun et al., 2010) tested different initial models in surface wave inversion, especially the uniform starting models, and their results have shown that the initial model will not affect the inversion results much, as long as the layers are dense enough. Fig. 8 shows the convergence of the model after different iterations in the inversion process.

Fig. 9 shows the sensitivity kernels of Rayleigh wave group velocity at different periods, and Fig. 10 shows horizontal maps of shear wave velocity structures at different depths. The pattern of shear wave velocity distribution in Guangzhou is consistent with the Rayleigh wave group velocity distribution in Fig. 7. The demarcation interface between high and low velocity indicates the location of the NE-SW GCF. There is an evident low-velocity anomaly along the GCF trace, which correlate with the depression basins along the fault. Around the GCF, there are high-velocity anomalies at the northern part of Guangzhou,

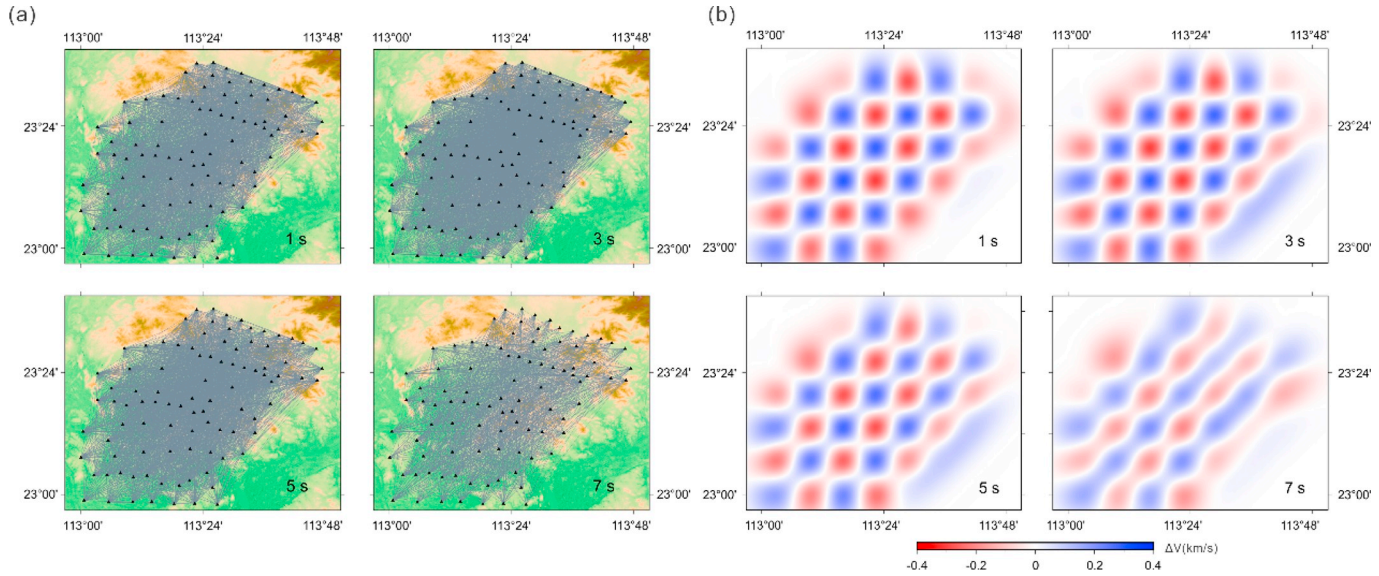

Fig. 6. (a) Ray path recovery and (b) checkerboard test of Rayleigh wave group velocity at different periods. The period for each panel is labeled on the lower right corner. (a) Black triangles represent seismic stations. (b) The input model has 0.1° by 0.1° grid and the velocity perturbation is 0.4 km/s.

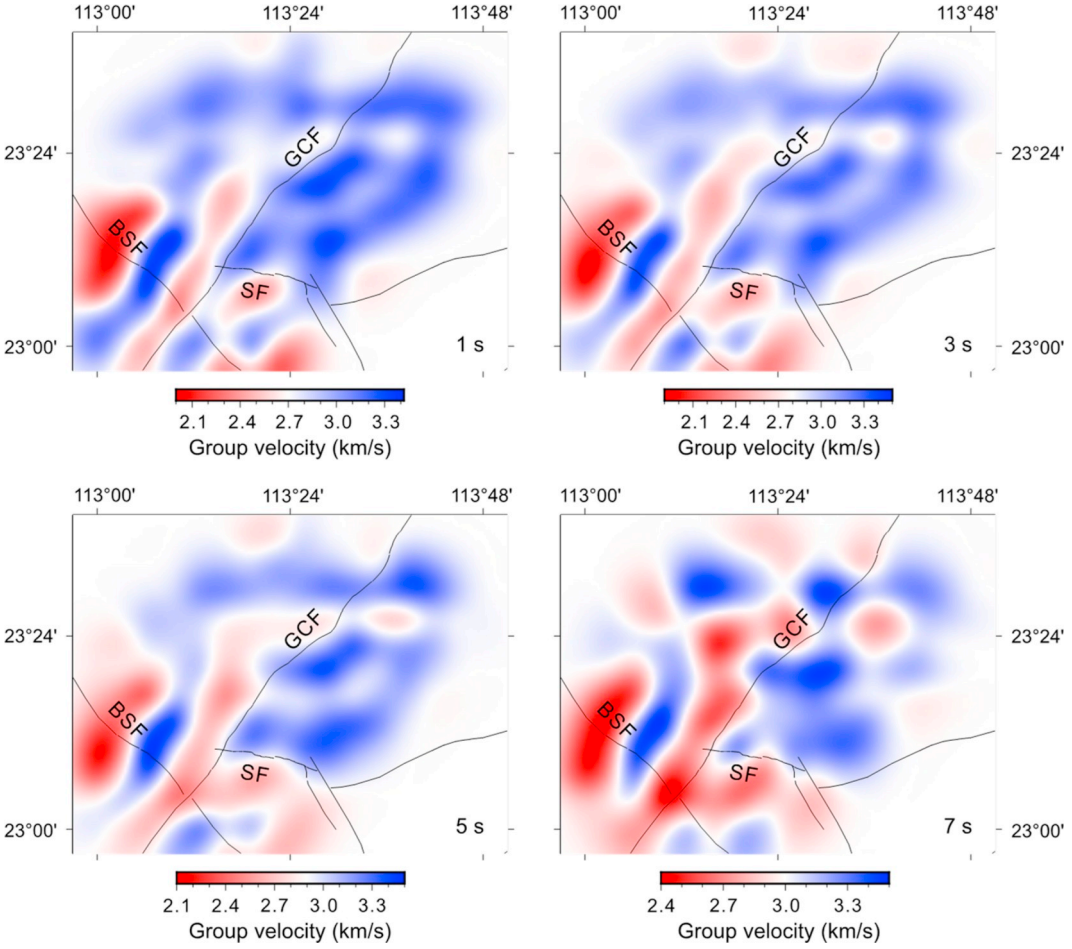

Fig. 7. Maps of Rayleigh wave group velocity at different periods. The faults (black lines) are also plotted. The period for each panel is labeled on the lower right corner.

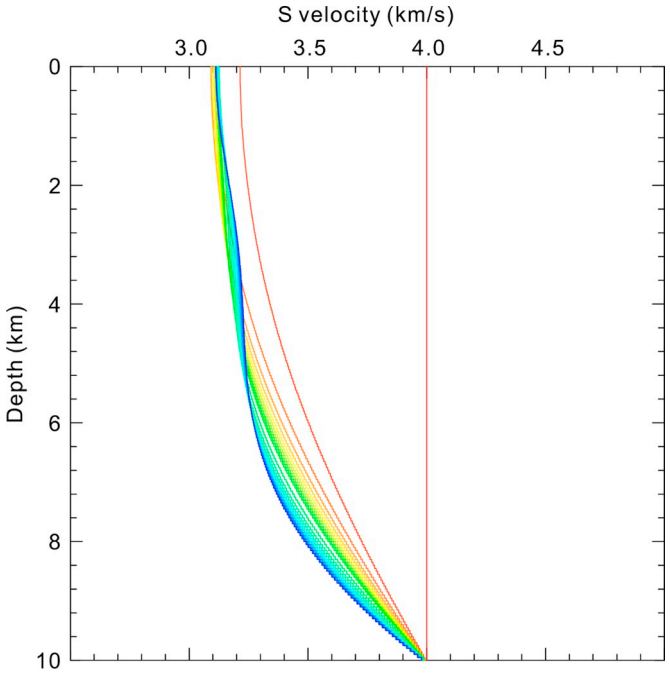

Fig. 8. Example of the convergence of the model in the inversion. The red and blue lines are the initial and final models, respectively. This example uses the same group velocity observation in the grid at the center of the study area, as shown in Fig. 9. (For interpretation of the references to colour in this figure legend, the reader is referred to the web version of this article.)

which persist from surface to at least 6 km. At shallow depth ($\leq$3.5 km), the SF divides the southeastern part of GCF into two blocks: The northern part of the SF is characterized by high velocity and the southern part generally shows low velocity. The high velocities to the north of the SF are correlated with the Mountains of Guangzhou, while the low velocities to the south of the SF correlate with the sediment basins. At 6 km depth, most of the area is characterized by low-velocity anomalies.

Several cross sections perpendicular to the faults are presented in Fig. 11. In profile AA', BB' and CC', obvious low-velocity anomalies appear on the west side of the GCF (depressed basins). In cross section AA' and BB', the GCF presents a nearly vertical dip. However, in CC', two low velocity blocks are connected, and the GCF has no clear dip direction in this cross section. In section DD', the SF divides this section into high velocity in the north (mountain area) and low velocity in the south (sediment basin). The interface of high and low velocity anomalies inclines southward at an angle of nearly 60 degrees. The depth of this low velocity extends to about 6 km.

4. Near-surface structures and Site effect assessment from Horizontal to vertical spectral ratio (HVSR) across the SF

Ambient noise tomography (ANT) results of Guangzhou can image the general faults and tectonic blocks in the area. However, its resolution is still not good enough to image the fine structures of the faults and the sedimentary layers. To better understand the characteristics of the SF, which is one of the most important faults transverse the city, we deployed another dense linear array perpendicular to it. We use HVSR method to investigate the fault position as well as the sedimentary amplification in its vicinity.

The HVSR method was originally proposed by Borcherdt (Borcherdt, 1970) and then improved by Nakamura (Nakamura, 1989) and Lermo and Chavez-Garcia (Chávez-García and Lermo, 1993). It gives good estimation of sediment thickness and site amplification from the ground soil resonance frequency, and thus frequently used in

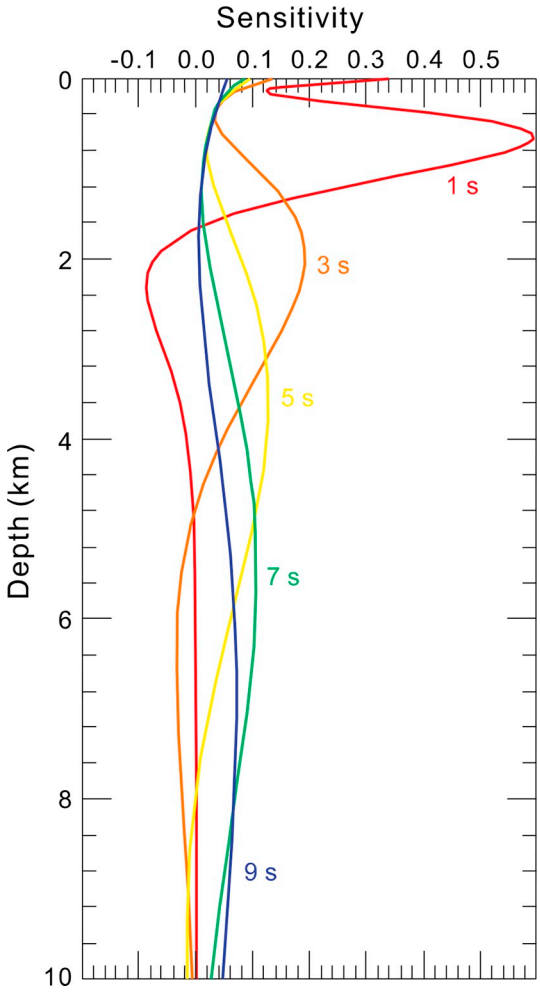

Fig. 9. Sensitivity kernels of Rayleigh wave group velocity to the shear wave velocity at different periods.

engineering seismology (Bao et al., 2018; Chen et al., 2009; Liu et al., 2014; Luthfiyani et al., 2019; Mundepi and Mahajan, 2010; Panou et al., 2005; Picotti et al., 2017; Wohlenberg and Ibs-von Seht, 1999).

We select 2-hour time length continuous data of each day, from 1 to 3 AM, to calculate the HVSR curves. At this time period, human activities are least and thus we can avoid contaminations from specific sources. In the calculation, we also use an anti-triggering short-term to long-term window (STA/LTA) algorithm to stabilize the signal. Then we process the data as follows: (1) We cut the selected 2-hour data of each day into 30s time windows, with 30% overlapping time between adjacent windows; (2) The HVSR curves are calculated in each time window, and Konno-Ohmachi smoothing algorithm (Konno and Ohmachi, 1998) is used in this process; (3) All time windows' HVSR curves are stacked to get the final one. These data are processed using the Geopsy software package (www.geopsy.org).

Further quality control eliminate HVSR curves with unclear peaks, mostly induced by traffic noise. Finally, we extract resonant frequency from 29 HVSR curves. A plot of the HVSR curves is shown in Fig. 12.

Fig. 13 are the HVSR resonant peak frequencies (f) and the corresponding amplification magnitudes (A) for all stations. Note that we just use the amplitude of HVSR to characterize the amplification factor while its amplitude does not indicate the absolute amplification at the location of the measurements (Rong et al., 2017). It is noticeable that there are high-amplitude points at about 1800–1900 m. K-value (A^2/f) of ground and structures, which is considered as an index for the vulnerability of ground destruction (Nakamura, 1997), is also plotted in Fig. 13(c). Most sites of this region have a K-value below 20. It is

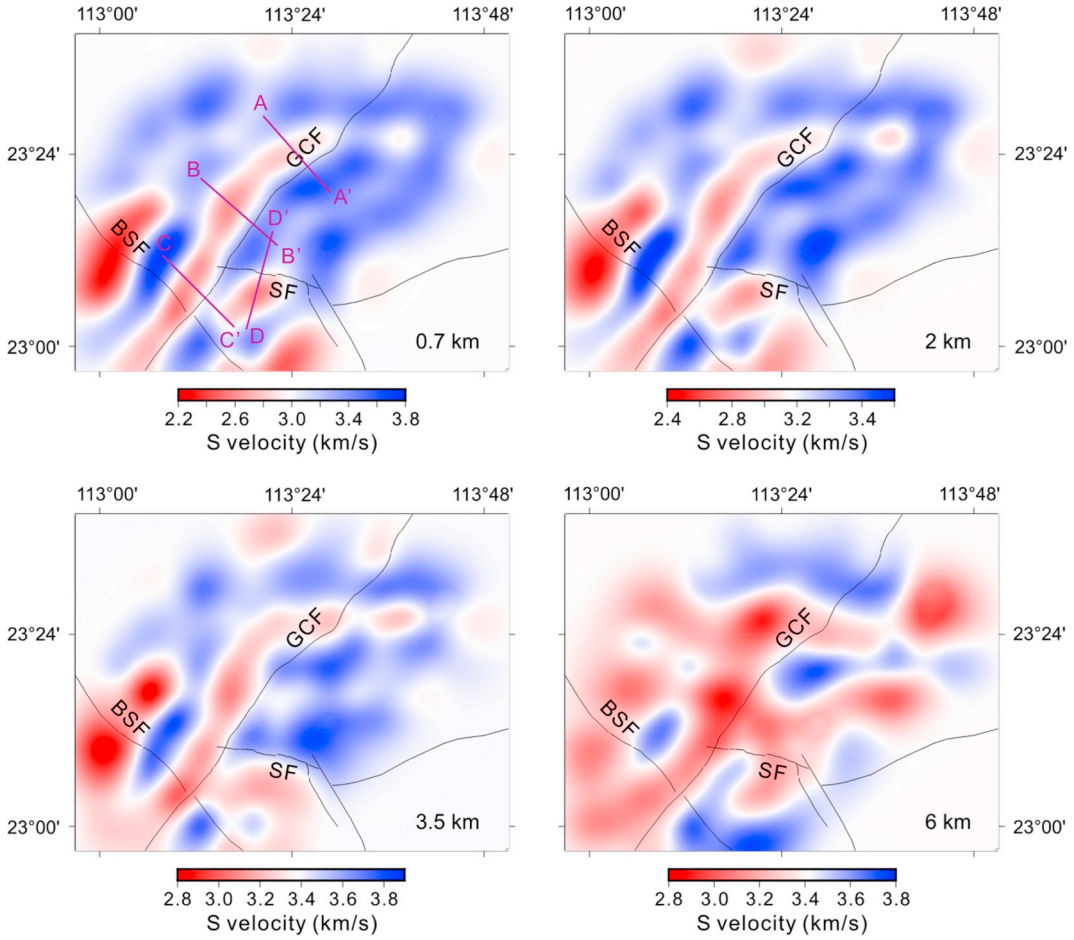

Fig. 10. Maps of inverted shear wave velocity at depths of 0.7, 2.0, 3.5, and 6 km. The depth for each figure is labeled on the lower right corner. The cross-section of the shear wave velocity profiles for the four magenta lines (AA', BB', CC' and DD') in the upper-left panel are shown in Fig. 11.

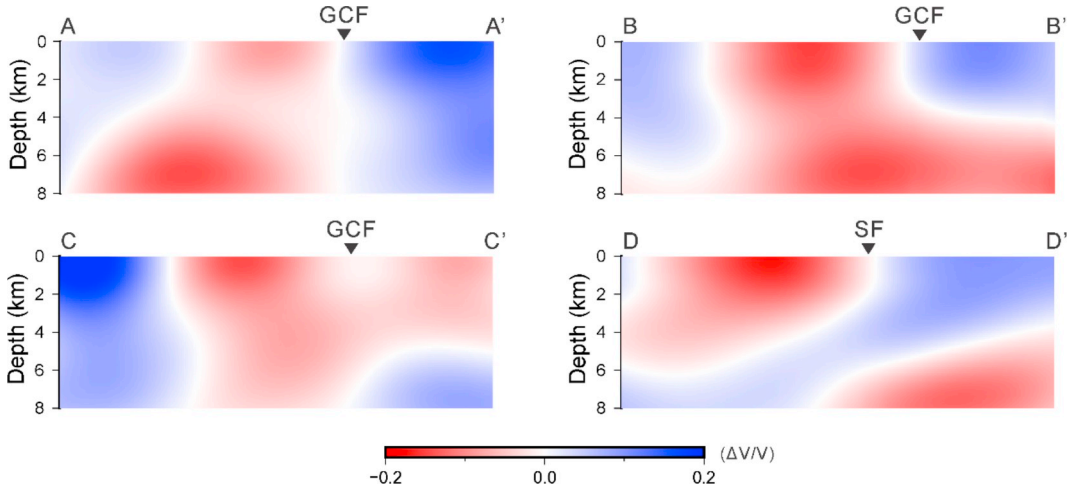

Fig. 11. The shear wave velocity variations of four cross sections (location shown in Fig. 1 and Fig. 10). Black triangles indicate the fault locations.

noteworthy to point out that extremely high K-values appear at about 1800–1900 m.

There are two commonly used empirical relationship between HVSR peak resonant frequency (f_r) and the sediment thickness (h): $h = 96f_r^{-1.388}$ and $h = 108f_r^{-1.551}$ (Chen et al., 2009; Ibs-von Seht and Wohlenberg, 1999; Liu et al., 2014; Parolai et al., 2002). The resonant frequency of the sedimentary layer in Guangzhou is generally greater than 1 Hz. We compare thickness of sediment calculated by these two empirical formulas and find that there is little difference between these two results. Moreover, we also select several drilling holes and compare their sediment thicknesses with the results calculated from the nearby stations (Table 1). Based on the fitness of calculated results, we prefer to use $h = 96f_r^{-1.388}$ to obtain the sediment thickness in Guangzhou (Fig. 14b).

Based on the HVSR data, we then use the OpenHVSR (Bignardi et al., 2016) to invert 2-D near-surface shear wave velocity beneath this dense array. We use the following equation as objective function to find the best velocity model:

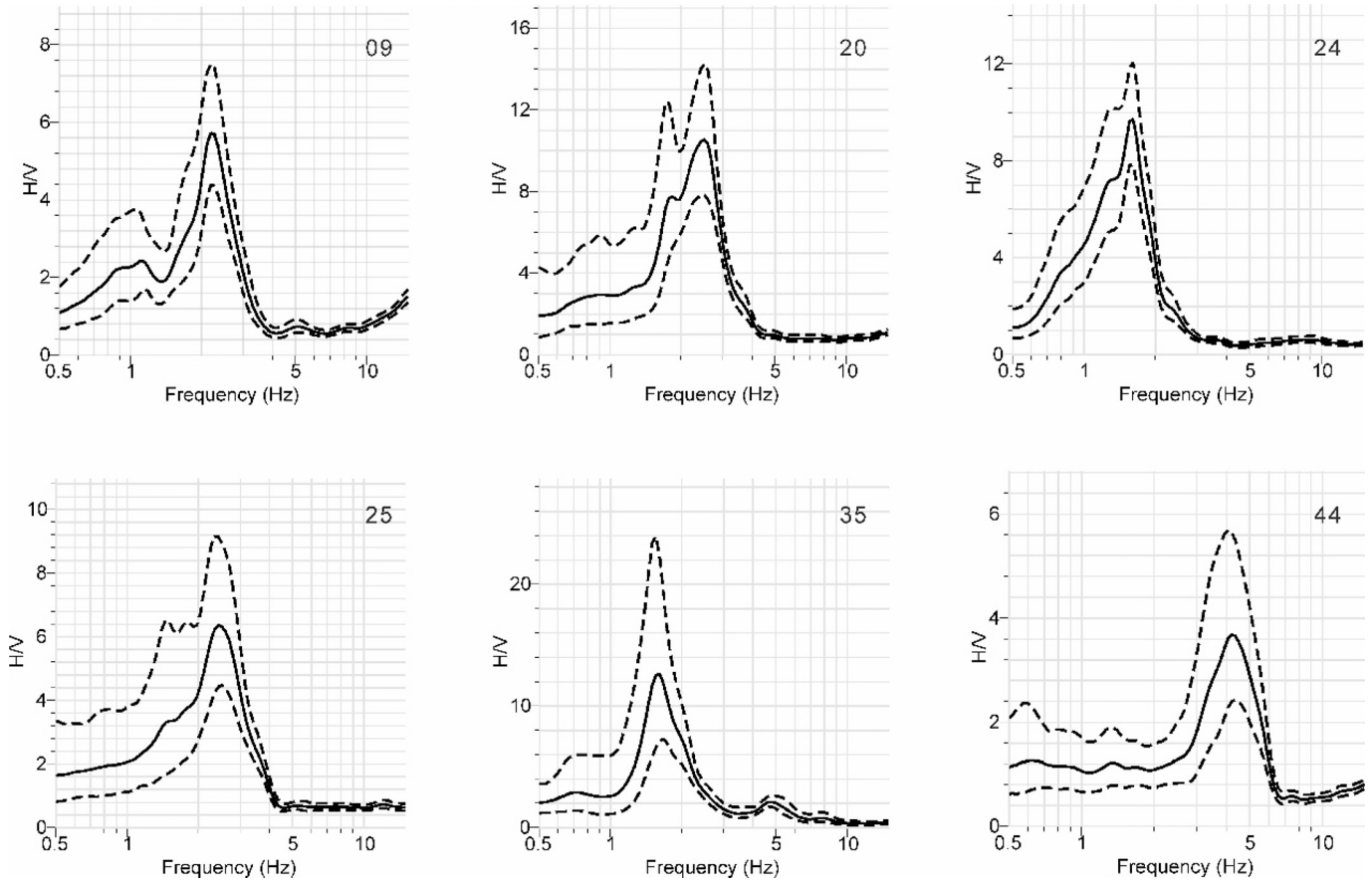

Fig. 12. Example of HVSR curves at six stations (location shown in Fig. 2). Solid curves represent the final stack of HVSR curves and broken curves represent mean square error of HVSR stacks. The station number is labeled on the upper right corner.

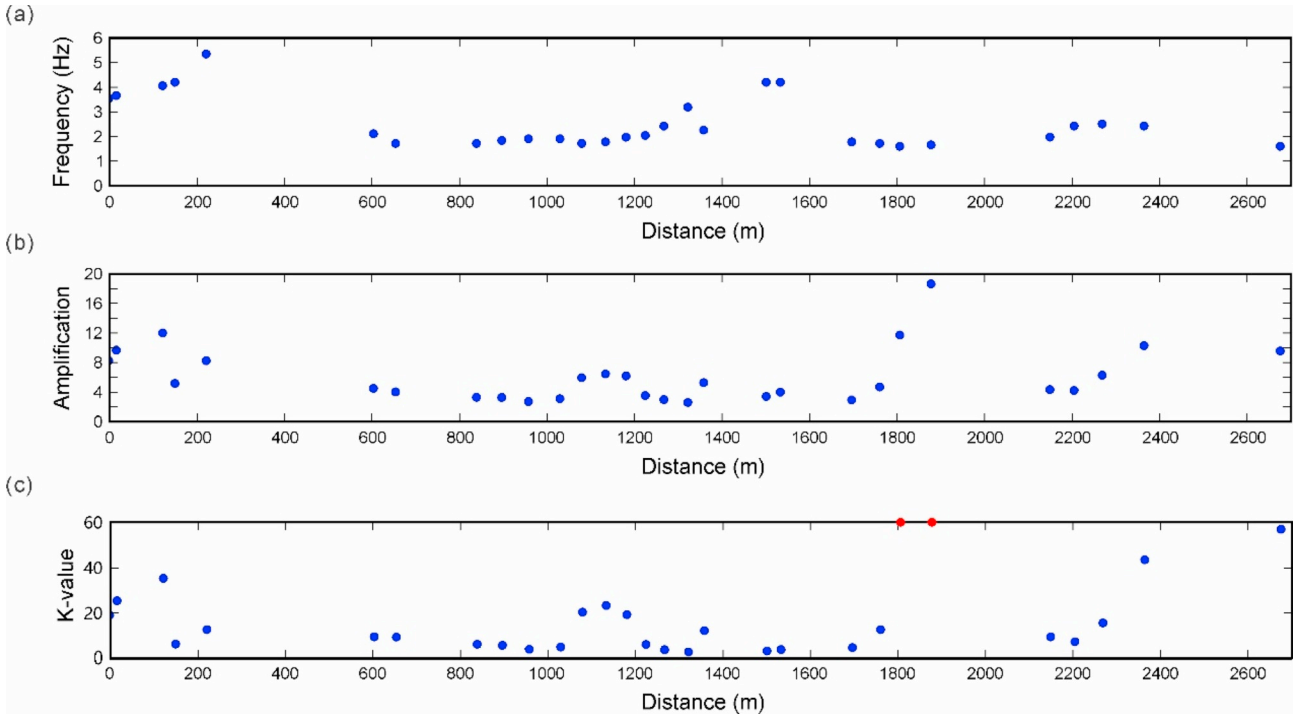

Fig. 13. The map of (a) peak resonance frequency (in Hz) distribution, (b) amplification factor of HVSR at the peak resonance frequency and (c) seismic vulnerability of the ground (the K-value) along the linear array. The two red points in (c) represent extremely high K-values greater than 80. (For interpretation of the references to colour in this figure legend, the reader is referred to the web version of this article.)

Table 1
Comparison of sediment thickness obtained by borehole and HVSR method using two different formulas. The location of these boreholes and stations are shown in Figs. 1 and 2.

Borehole	Sediment thickness (m) from borehole	Station	Sediment thickness (m) from station using $h = 96f_r^{-1.388}$	Sediment thickness (m) from station using $h = 108f_r^{-1.551}$
CZS	28.5	47	33.18	33.76
HJC	14.1	07	14.78	13.35
ZK2841	5.16	GZ038	5.13	6.95
DS0994	10.80	GZ073	10.20	8.82
DS3929	22.00	GZ070	22.76	21.63

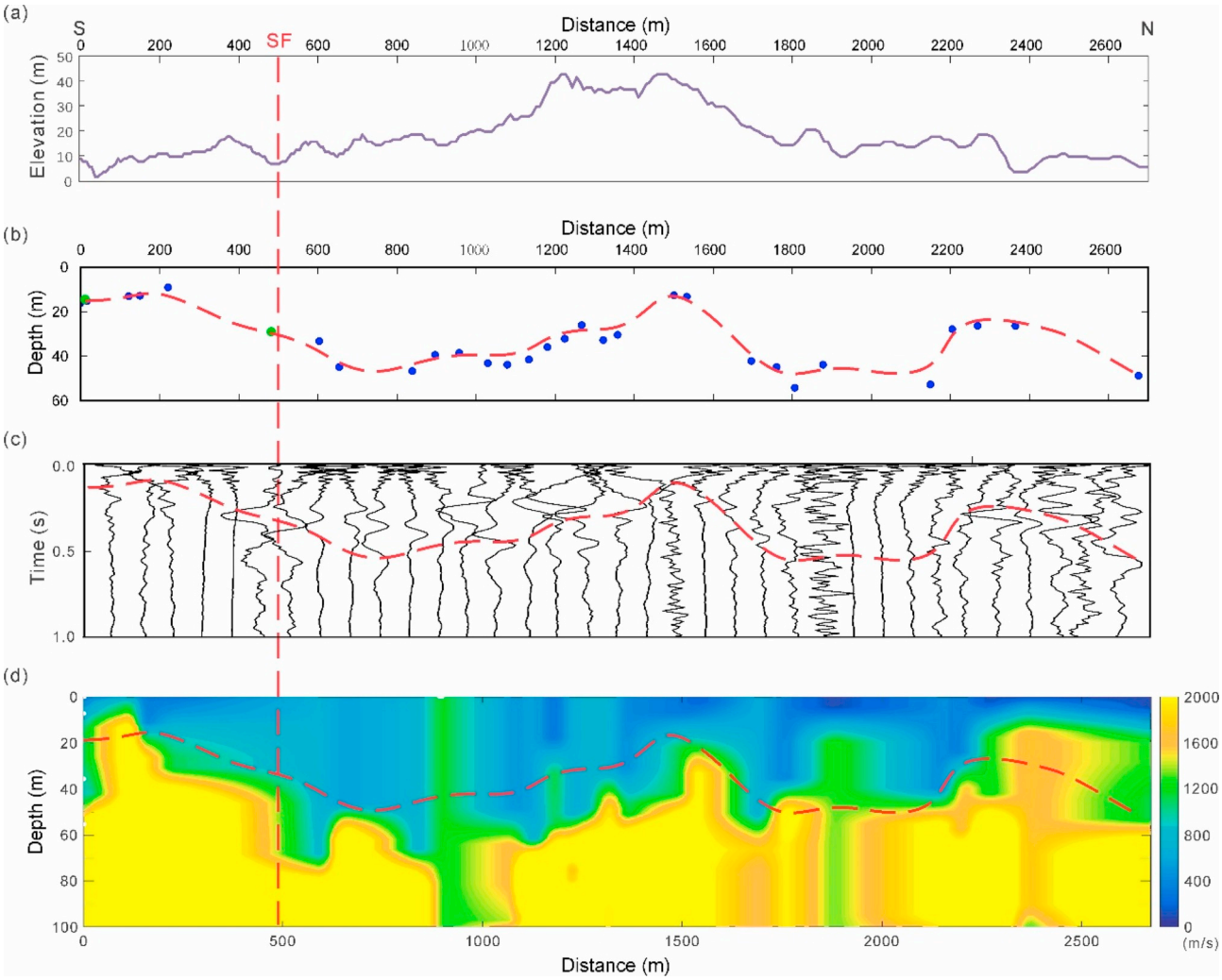

Fig. 14. (a) Surface elevation profile along the SFL. (b) Sediment thickness profile from the HVSR method. The best fitted interface is shown as the red dashed curves with superimposing on (c) and (d). The borehole data CZS and HJC in Fig. 2 are also plotted with green dots. (c) The "pseudo-reflection" profile obtained from 1-spacing cross-correlation with the superposition of the sediment thickness (the broken curve) obtained from HVSR in (b). (d) Shear wave velocity profile along the SFL inverted from HVSR superimposed with the sediment thickness (the broken curve) obtained from HVSR in (b). The vertical dashed line indicates the sharp changes of elevation and velocities in where the Shougouling Fault intersects the SFL. (For interpretation of the references to colour in this figure legend, the reader is referred to the web version of this article.)

Table 2
Parameters in the initial model for 2D shear wave velocity inversion from HVSR curves.

Layer	V_P (m/s)	V_S (m/s)	H (m)	ρ (kg/m^3)	Q_P	Q_S
1	200	100	10	1.8	15	5
2	300	200	15	1.8	30	20
3	500	300	15	1.8	30	20

$$E(\mathbf{m}) = aM(\mathbf{m}) + bS(\mathbf{m}) + \sum_{j=1}^{5} a_j R_j(\mathbf{m})$$

Where $M(\mathbf{m})$ represents the misfit between data and the simulated curves; $S(\mathbf{m})$ represents a noval forcing condition on the slope of the curves and $R_j(\mathbf{m})$ is a regularizing term. Its global minimum is searched.

Table 2 shows the initial model of the inversion. We test different initial models, and find that after many iterations, it generally will converge to similar results. The final results are plotted in Fig. 14.

Fig. 14 shows the major results on tectonic implications along the SF

profile. The sediment depth profile derived from the peak resonance frequencies (Fig. 14b) displays a good correlation with the surface elevation (Fig. 14a). It is worth noting that there is an increase in sediment thickness near 400–500 m along the SFL. According to the rapid increase of sediment thickness and the drop of the surface elevation, we infer that this is where the SF transverse across. The thickness here is also consistent with the CZS borehole data (Table 1).

We fit a curve to the sediment depth data and then put it on the "pseudo-reflection" profile obtained from cross-correlation (Fig. 14c) and shear wave velocity profile inverted by HVSR data (Fig. 14d). The 'pseudo-reflection' profile is formed by stacking of cross-correlations of seismic records between two adjacent sites. The data processing procure is similar to ambient noise tomography from the beginning to the stacking process described in Section 3. The vertical-component data of each station was cut into 5 s segments and then cross-correlation is performed between the adjacent sites. The cross-correlations after stacking are arranged along the actual deployment order of the stations, and the "pseudo-reflection" profile is achieved. There is good consistency between the "pseudo-reflection" and the sediment thickness variation. Moreover, the shear wave velocity profile basically has a consistent trend of variation with the sediment thickness.

5. Discussion

From the tomography results, it is clear that the NE-SW trending GCF possesses a nearly vertical dip angle. However, previous geological observations of the outcrop showed that the GCF inclines to NW at the northern segment (Ma et al., 2007; Pan, 1992). Nevertheless, the inclination in the southern part of the GCF is unknown because of the thick sediments above it. Actually, the GCF is the final product of a series of multi-stage tectonic movements, including the tectonic stages in the Mesozoic era and Cenozoic era (Yan, 1989). Originally the GCF was formed in the Triassic period, and its strike coincides with the entire Guanghua Triassic fault-fold zone and dips to NW (Yan, 1989). Subsequently, active tectonic movements in the Jurassic period and Cretaceous period formed a series of large-scale NE-NNE trending rupture belts, which generally dips to SE (Yan, 1989). We infer that the tectonic movements in the Jurassic period and Cretaceous period may altered the dip direction of GCF in the deep depth. To the west side of the GCF, the Taipingchang depression and the Longgui basin are distributed along the fault as well, and their general orientation and internal structures are consistent with the fault (Yan, 1989). Moreover, the distribution of hot springs in the northern part of the GCF also confirms the location of the fault, since underground hot water can easily gushes out from granite fractures (Yan, 1989).

On the east side of the GCF, the deep metamorphic rocks of the Lower Paleozoic, such as the Maofeng Mountain and the Baiyun Mountain, are exposed in large areas. At deep depth ($>$ 4 km), the low-velocity anomalies beneath BB' and DD' (Fig. 11) may indicate that the mountain bodies gradually disappear. High-velocity anomalies are consistent with this surface geological structures. Similarly, large mountainous areas in the northern part of the study area are characterized by high-velocity anomalies, too.

For the SF, the demarcation interface between high velocity in the north and low velocity in the south reveals a south dip direction. The SF is a normal fault and it has experienced many periods of multi-stage activities (Yan, 1985). The base of the Pearl River Delta in the south of the SF is a fault-controlled basin. Previous geological studies show that the Cretaceous-Lower Tertiary red rocks deposited in the Mesozoic and Cenozoic in fault basins is up to 4–5 km thick (Zhao, 1982) and the depth of the southern low velocity in our results is generally consistent with this thickness (Fig. 11d). The alluvial plain and the development of rivers in the southern part of the SF is also characterized with low-velocity anomalies. From Fig. 14(b), we notice a thinner sedimentary layer at the hanging wall of the SF from 0 to 400 m distance along the SFL. At about 500 m distance along the SFL, the elevation drops and the sediment layer from south to north becomes thicker. The thinner sedimentary layer is contradictory with the property of normal fault that the hanging wall should has a thicker sedimentary layer. We suggest that the SF experienced a temporal reverse and the northern part of it is a small basin with a thicker sediment layer. Since the Miocene, the SF has experienced many opposite movements. Its mechanical properties are characterized by alternating NS tension and compression, mainly by NS tension (Yan, 1985). The SF may become a reverse fault when the NS compression was dominant, and formed a compressional basin. At the same time, the northward pressure prompted a rise in the middle of the basin (at about 1200–1600 m distance along SFL), and the stress state changed to tensile. The fault then turned over into a normal fault, and the sediment layer structure reverse on the southern margin of the basin.

The site effects (Fig. 13) can be used to investigate the vulnerability of infrastructures and surface ground. The majority of the low K-values indicate relatively small risks of ground shaking along the Hua-nan Expressway. The extremely high K-values from 2 points at about 1800–1900 m of the profile (Fig. 13c) may indicate a great potential of structure damage. These sites turn out to be near a pond and have thick sediments, and thus caution must be taken in constructions near these locations. Overall, except these two points, the vulnerability at the fine scale along this array, the peak resonance frequencies (between 1 Hz and 5 Hz, Fig. 13a), and sediment thicknesses (from 15 m to 40 m, Fig. 14d) are all consistent with those in Zong et al. (Zong et al., 2020).

In fact, the faulting activity in Guangzhou area is relatively weak. Since Holocene, modern cross-fault topographic deformation observations show that its activity level is low, and it is unlikely to cause strong earthquakes (Chen et al., 2000). However, the degree of damage does not only increase in proportional to the local earthquake magnitude. It is also affected by many other factors, such as the surrounding geological structures, soil characteristics and building vulnerability. Small local earthquakes or strong tele-earthquakes can also lead to great damage when the near-surface amplification effect is strong. Caution must be taken at areas with high risks (K-value).

We have obtained the 3-D structures and distinguished the distribution of the major faults in Guangzhou area. The GCF is the most important fault and has a great possibility of earthquake occurrence (Pan, 1992; Zhou et al., 2009). Therefore, we suggest that in the process of urban construction, engineering construction and underground space exploitation should be avoided in the GCF area, especially near its intersection zone with the SF; or higher standards must be set for buildings and infrastructure design.

6. Conclusions

Ambient noise tomography and HVSR analysis have been successfully applied for metropolitan Guangzhou area. At shallow depths, the 3-D sub-surface structures show obvious features that consistent with surficial geology; e.g., high velocities are beneath the mountain area and low velocities are beneath the alluvial and basin regions. Moreover, our results depict clear fault geometries, such as the GCF and SF locations and dip angles. At the same time, HVSR results from a dense array along the Hua-nan Expressway reveal clear change of the sediment thickness across the SF. The low risks of potential damage along the array are also supported by low K-values. This work provides important constraints in understanding the geological tectonics, the fault geometry, and site effect estimation in metropolitan Guangzhou. The distribution of faults and sediments, as well as risk map not only help to mitigate earthquake hazards, but also provide valuable information for urban planning and infrastructure construction.

Declaration of Competing Interest

The authors declare that they have no known competing financial interests or personal relationships that could have appeared to influence the work reported in this paper.

Acknowledgement

This work is supported by Science and Technology Program of Guangzhou, China (No. 201707020029), DREAM project of the National Key R&D Program of China (No. 2016YFC0600402) and the program of China Scholarship Council (No. 201804910489). We would like to thank anonymous reviewers and the editors for their constructive comments on our manuscript.

References

Bao, F., Li, Z., Yuen, D.A., Zhao, J., Ren, J., Tian, B., Meng, Q., 2018. Shallow structure of the Tangshan fault zone unveiled by dense seismic array and horizontal-to-vertical spectral ratio method. Phys. Earth Planet. Inter. 281, 46–54. https://doi.org/10.1016/j.pepi.2018.05.004.

Bensen, G.D., Ritzwoller, M.H., Barmin, M.P., Levshin, A.L., Lin, F., Moschetti, M.P., Shapiro, N.M., Yang, Y., 2007. Processing seismic ambient noise data to obtain reliable broad-band surface wave dispersion measurements. Geophys. J. Int. 169, 1239–1260. https://doi.org/10.1111/j.1365-246X.2007.03374.x.

Bignardi, S., Mantovani, A., Abu Zeid, N., 2016. OpenHVSR: imaging the subsurface 2D/3D elastic properties through multiple HVSR modeling and inversion. Comput. Geosci. 93, 103–113. https://doi.org/10.1016/j.cageo.2016.05.009.

Boatwright, J., Fletcher, J.B., Fumal, T.E., 1991. A general inversion scheme for source, site, and propagation characteristics using multiply recorded sets of moderate-sized earthquakes. Bull. Seismol. Soc. Am. 81, 1754–1782.

Borcherdt, R.D., 1970. Effects of local geology on ground motion near San Francisco Bay*. Bull. Seismol. Soc. Am. 60, 29–61.

Brantley, B.J., Chung, W.-Y., 1991. Body-wave waveform constraints on the source parameters of the Yangjiang, China, earthquake of July 25, 1969: A devastating earthquake in a stable continental region. Pure Appl. Geophys. 135, 529–543. https://doi.org/10.1007/BF01772404.

Campillo, M., Paul, A., 2003. Long-range correlations in the diffuse seismic coda. Science 299, 547–549. https://doi.org/10.1126/science.1078551.

Chávez-García, F.J., Lermo, J., 1993. Site effect evaluation using spectral ratios with only one station. Bull. Seismol. Soc. Am. 83, 1574–1594.

Chen, W.-G., Zhao, H.-M., Chang, Y., 2000. Features of active faults in Guangzhou region and relation to earthquake resistant engineering. South China. J. Seismol. 20, 47–56. https://doi.org/10.13512/j.hndz.2000.02.010.

Chen, Q., Liu, L., Wang, W., Rohrbach, E., 2009. Site effects on earthquake ground motion based on microtremor measurements for metropolitan Beijing. Chin. Sci. Bull. 54, 280–287. https://doi.org/10.1007/s11434-008-0422-2.

Cheng, J.-J., 2012. Research on ground collapse characteristics of guangzhou and control countermeasures. J. Railw. Eng. Soc. 29, 1–5.

Cheng, C., Chen, L., Yao, H., Jiang, M., Wang, B., 2013. Distinct variations of crustal shear wave velocity structure and radial anisotropy beneath the North China Craton and tectonic implications. Gondwana Res. 23, 25–38. https://doi.org/10.1016/j.gr.2012.02.014.

Dai, J., 2015. Site effects analysis of wenchuan earthquake by using microtremor and strong motion observation data. Recent Dev. World Seismol. 4, 37–38. https://doi.org/10.3969/j.issn.0235-4975.2015.04.008.

Deng, Z., 2016. Main fracture characteristics of guangzhou city and impact on urban construction. Urban Geotech. Invest. Surv. 161–166.

Geng, G., 2015. Study on site effect based on data of seismic array. Recent Dev. World Seismol. 3, 46–47. https://doi.org/10.3969/j.issn.0235-4975.2015.03.010.

Gosar, A., Martinec, M., 2008. Microtremor HVSR study of site effects in the ilirska bistrica town area (S. Slovenia). J. Earthq. Eng. 13, 50–67. https://doi.org/10.1080/13632460802212956.

Herrmann, R.B., 2013. Computer programs in seismology: an evolving tool for instruction and research. Seismol. Res. Lett. 84, 1081–1088. https://doi.org/10.1785/0220110096.

Huang, Y.C., Yao, H., Huang, B.S., van der Hilst, R.D., Wen, K.L., Huang, W.G., Chen, C.H., 2010. Phase velocity variation at periods of 0.5-3 seconds in the Taipei Basin of Taiwan from correlation of ambient seismic noise. Bull. Seismol. Soc. Am. 100, 2250–2263. https://doi.org/10.1785/0120090319.

Ibs-von Seht, M., Wohlenberg, J., 1999. Microtremor measurements used to map thickness of soft sediments. Bull. Seismol. Soc. Am. 89, 250–259.

Jolly, A.D., Lokmer, I., Kennedy, B., Keys, H.J.R., Proctor, J., Lyons, J.J., Jolly, G.E., 2014. Active seismic sources as a proxy for seismic surface processes: an example from the 2012 Tongariro volcanic eruptions, New Zealand. J. Volcanol. Geotherm. Res. 286, 317–330. https://doi.org/10.1016/j.jvolgeores.2014.04.008.

Konno, K., Ohmachi, T., 1998. Ground-motion characteristics estimated from spectral ratio between horizontal and vertical components of microtremor. Bull. Seismol. Soc. Am. 88, 228–241.

Li, H., Chen, L., Li, Y., 2008. Numerical simulation of active faults in guangzhou area. J. Geodesy Geodyn. 28, 39–44. https://doi.org/10.14075/j.jgg.2008.02.020.

Li, C., Yao, H., Fang, H., Huang, X., Wan, K., Zhang, H., Wang, K., 2016a. 3D Near-surface shear-wave velocity structure from ambient-noise tomography and borehole data in the Hefei Urban Area, China. Seismol. Res. Lett. 87, 882–892. https://doi.org/10.1785/0220150257.

Li, Z., Ni, S., Zhang, B., Bao, F., Zhang, S., Deng, Y., Yuen, D.A., 2016b. Shallow magma chamber under the Wudalianchi Volcanic Field unveiled by seismic imaging with dense array. Geophys. Res. Lett. 43, 4954–4961. https://doi.org/10.1002/2016gl068895.

Lin, F.-C., Li, D., Clayton, R.W., Hollis, D., 2013. High-resolution 3D shallow crustal structure in Long Beach, California: Application of ambient noise tomography on a dense seismic array. Geophysics 78, Q45–Q56. https://doi.org/10.1190/geo2012-0453.1.

Liu, L., 2001. Stable continental region earthquakes in South China. Pure Appl. Geophys. 158, 1583–1611. https://doi.org/10.1007/PL00001235.

Liu, L., Chen, Q.-F., Wang, W., Rohrbach, E., 2014. Ambient noise as the new source for urban engineering seismology and earthquake engineering: a case study from Beijing metropolitan area. Earthq. Sci. 27, 89–100. https://doi.org/10.1007/s11589-013-0052-x.

Liu, H.-P., Pan, A.-D., Wang, Y.-L., Luo, L.-F., 2004. Geological disaster in Guangdong Province and their prevention and control. J. Nat. Disasters 13, 101–105. https://doi.org/10.13577/j.jnd.2004.0218.

Liu, H.-P., Wang, Y.-L., Liu, J.-L., Ni, Y.-X., Wang, J.-J., Liang, H.-M., 2005. Cause mechanism and spatiotemporal distribution of major geological disasters in Guangzhou. J. Nat. Disasters 14, 153–157. https://doi.org/10.13577/j.jnd.2005.0527.

Liu, J.-L., Liu, H.-P., Liu, W.-J., 2007a. Study on ground collapse risk evaluation in Ma in Urban Area of Guangzhou City. J. Disaster Prevent. Mitigation Eng. 27, 488–492. https://doi.org/10.13409/j.cnki.jdpme.2007.04.007.

Liu, J.-L., Liu, W.-J., Wu, X.-B., Liu, H.-P., 2007b. GIS - based hazard appraisement of ground collapse in downtown area of Guangzhou city. J. Eng. Geol. 15, 630–634.

Lobkis, O.I., Weaver, R.L., 2001. On the emergence of the Green's function in the correlations of a diffuse field. J. Acoust. Soc. Am. 110, 3011–3017. https://doi.org/10.1121/1.1417528.

Luthfiyani, N., Yudistira, T., Rexha, V.R., 2019. Shear Velocity (VS) Estimation with HVSR (Horizontal to Vertical Spectrum Ratio) Curve Inversion Method of Microtremor Measurement in Bandung Basin. IOP Conf. Ser. 318, 012034. https://doi.org/10.1088/1755-1315/318/1/012034.

Ma, H., Wu, Y., Chen, P., Guo, L., Guo, Q., 2007. The latest activity of Feilailing-Xianggangshan segment in Guangzhou-Conghua fault. Technol. Earthq. Disaster Prevent. 2, 339–345.

Mundepi, A.K., Mahajan, A.K., 2010. Site response evolution and sediment mapping using horizontal to vertical spectral ratios (HVSR) of ground ambient noise in Jammu city, NW India. J. Geol. Soc. India 75, 799–806. https://doi.org/10.1007/s12594-010-0070-4.

Nakamura, Y., 1989. A Method for Dynamic Characteristics Estimation of Subsurface Using Microtremor on the Ground Surface. 30. Quarterly Report of RTRI (Railway Technical Research Institute) (Japan), pp. 25–33.

Nakamura, Y., 1997. Seismic Vulnerability Indices for Ground and Structures Using Microtremor. World Congress on Railway Research, Florence.

Pan, J., 1992. Seismogenic structure in Guangzhou area and its seismic risk. South China J. Seismol. 12, 32–41.

Pan, H., Yan, J., Zhang, Z., Li, B., Li, J., Hao, Y., 2009. Review on 1918 Nan'ao Ms7.3 earthquake and its strong aftershocks. Technol. Earthq. Disaster Prevent. 4, 40–48. https://doi.org/10.3969/j.issn.1673-5722.2009.01.004.

Panou, A.A., Theodulidis, N., Hatzidimitriou, P., Stylianidis, K., Papazachos, C.B., 2005. Ambient noise horizontal-to-vertical spectral ratio in site effects estimation and correlation with seismic damage distribution in urban environment: the case of the city of Thessaloniki (Northern Greece). Soil Dyn. Earthq. Eng. 25, 261–274. https://doi.org/10.1016/j.soildyn.2005.02.004.

Parolai, S., Bormann, P., Milkereit, C., 2002. New relationships between vs, thickness of sediments, and resonance frequency calculated by the H/V ratio of seismic noise for the Cologne Area (Germany). Bull. Seismol. Soc. Am. 92, 2521–2527. https://doi.org/10.1785/0120010248.

Picotti, S., Francese, R., Giorgi, M., Pettenati, F., Carcione, J.M., 2017. Estimation of glacier thicknesses and basal properties using the horizontal-to-vertical component spectral ratio (HVSR) technique from passive seismic data. J. Glaciol. 63, 229–248. https://doi.org/10.1017/jog.2016.135.

Rawlinson, N., Sambridge, M., 2005. The fast marching method: an effective tool for tomographic imaging and tracking multiple phases in complex layered media. Explor. Geophys. 36, 341–350. https://doi.org/10.1071/eg05341.

Renalier, F., Jongmans, D., Campillo, M., Bard, P.-Y., 2010. Shear wave velocity imaging of the Avignonet landslide (France) using ambient noise cross correlation. J. Geophys. Res. 115. https://doi.org/10.1029/2009jf001538.

Rong, M., Fu, L.Y., Wang, Z., Li, X., Carpenter, N.S., Woolery, E.W., Lyu, Y., 2017. On the amplitude discrepancy of HVSR and site amplification from strong-motion observations. Bull. Seismol. Soc. Am. 107, 2873–2884. https://doi.org/10.1785/0120170118.

Snieder, R., 2004. Extracting the Green's function from the correlation of coda waves: A derivation based on stationary phase. Phys. Rev. E 69, 046610. https://doi.org/10.1103/PhysRevE.69.046610.

Sun, X., Song, X., Zheng, S., Yang, Y., Ritzwoller, M.H., 2010. Three dimensional shear wave velocity structure of the crust and upper mantle beneath China from ambient noise surface wave tomography. Earthq. Sci. 23, 449–463. https://doi.org/10.1007/s11589-010-0744-4.

Triantafyllidis, P., Hatzidimitriou, P.M., Suhadolc, P., 2002. 1-D Theoretical modeling for site effect estimations in thessaloniki: comparison with observations. Pure Appl. Geophys. 158, 2333–2347. https://doi.org/10.1007/978-3-0348-8177-7_4.

Triantafyllidis, P., Suhadolc, P., Hatzidimitriou, P.M., Anastasiadis, A., Theodulidis, N., 2004. PART I: theoretical site response estimation for microzoning purposes. Pure Appl. Geophys. 161, 1185–1203. https://doi.org/10.1007/s00024-003-2493-y.

Wang, S., Sun, X., Qin, J., He, L., Deng, Y., 2018. Fine fault structure of Xinfengjiang water reservoir area from high-frequency ambient noise tomography. Chin. J. Geophys. 61, 593–603. https://doi.org/10.6038/cjg2018L0434.

Wohlenberg, J., Ibs-von Seht, M., 1999. Microtremor measurements used to map

thickness of soft sediments. Bull. Seismol. Soc. Am. 89, 250–259.
Yan, G., 1985. The study of basic characteristics of fault-tectonic belts of Guangzhou-Luofushan and its formation and evolution. Acta Sci. Nat. Univ. Sunyatseni 24, 63–72.
Yan, G., 1989. Guangzhou-Conghua fault belt, its formation and evolution. Earth Sci. (Chikyu Kagaku) 43, 297–313.
Yang, Y., Ritzwoller, M.H., Levshin, A.L., Shapiro, N.M., 2007. Ambient noise Rayleigh wave tomography across Europe. Geophys. J. Int. 168, 259–274. https://doi.org/10.1111/j.1365-246X.2006.03203.x.
Yao, H., Xu, G., Zhu, L., Xiao, X., 2005. Mantle structure from inter-station Rayleigh wave dispersion and its tectonic implication in western China and neighboring regions. Phys. Earth Planet. Inter. 148, 39–54. https://doi.org/10.1016/j.pepi.2004.08.006.
Yao, H., Gouédard, P., Collins, J.A., McGuire, J.J., van der Hilst, R.D., 2011. Structure of young East Pacific rise lithosphere from ambient noise correlation analysis of fundamental- and higher-mode Scholte-Rayleigh waves. Compt. Rendus Geosci. 343, 571–583. https://doi.org/10.1016/j.crte.2011.04.004.
Yoon, S., Rix, G., 2009. Near-field effects on array-based surface wave methods with active sources. J. Geotech. Geoenviron. 135, 399–406. https://doi.org/10.1061/(ASCE)1090-0241(2009)135:3(399).
Zhao, H., 1982. The formation and evolution of the Pearl River Delta. Acta Oceanol. Sin. 4, 595–607.
Zhou, Q., Ran, H., Wu, Y., Chen, L., Li, H., 2009. Seismic hazard assessment of major faults in Guangzhou City. Technol. Earthq. Disaster Prevent. 4, 58–68.
Zong, J., Sun, X., Zhang, P., 2020. Site effect and earthquake disaster characteristics in Guangzhou area from horizontal-to-vertical spectral ratio (HVSR) method. Seismol. Geol.